

PAPER

Sufficient sampling for kriging prediction of cortical potential in rat, monkey, and human μ ECoG

To cite this article: Michael Trumpis *et al* 2021 *J. Neural Eng.* **18** 036011

View the [article online](#) for updates and enhancements.



PAPER

Sufficient sampling for kriging prediction of cortical potential in rat, monkey, and human μ ECoGRECEIVED
4 May 2020REVISED
15 November 2020ACCEPTED FOR PUBLICATION
16 December 2020PUBLISHED
8 March 2021Michael Trumpis¹ , Chia-Han Chiang¹ , Amy L Orsborn^{2,3,14,15} , Brinnae Bent¹ , Jinghua Li^{4,5,6}, John A Rogers^{4,7,8,9} , Bijan Pesaran² , Gregory Cogan^{10,11,12,13} and Jonathan Viventi^{1,10,13,16} ¹ Department of Biomedical Engineering, Duke University, Durham, NC 27708, United States of America² Center for Neural Science, New York University, New York, NY 10003, United States of America³ Department of Electrical & Computer Engineering, University of Washington, Seattle, WA 98195, United States of America⁴ Department of Materials Science and Engineering, Northwestern University, Evanston, IL 60208, United States of America⁵ Department of Materials Science and Engineering, The Ohio State University, Columbus, OH 43210, United States of America⁶ Chronic Brain Injury Program, The Ohio State University, Columbus, OH 43210, United States of America⁷ Simpson Querrey Institute, Northwestern University, Chicago, IL 60611, United States of America⁸ Department of Biomedical Engineering, Northwestern University, Evanston, IL 60208, United States of America⁹ Department of Neurological Surgery, Feinberg School of Medicine, Northwestern University, Chicago, IL 60611, United States of America¹⁰ Department of Neurosurgery, Duke School of Medicine, Durham, NC 27710, United States of America¹¹ Department of Psychology and Neuroscience, Duke University, Durham, NC 27708, United States of America¹² Center for Cognitive Neuroscience, Duke University, Durham, NC 27708, United States of America¹³ Duke Comprehensive Epilepsy Center, Duke School of Medicine, Durham, NC 27710, United States of America¹⁴ Department of Bioengineering, University of Washington, Seattle, Washington 98105, United States of America¹⁵ Washington National Primate Research Center, Seattle, Washington 98195, United States of America¹⁶ Department of Neurobiology, Duke School of Medicine, Durham, NC 27710, United States of AmericaE-mail: michael.trumpis@duke.edu**Keywords:** micro-electrocorticography, local field potential, spatial filter, spatial statistics, Gaussian processes, krigingSupplementary material for this article is available [online](#)**Abstract**

Objective. Large channel count surface-based electrophysiology arrays (e.g. μ ECoG) are high-throughput neural interfaces with good chronic stability. Electrode spacing remains ad hoc due to redundancy and nonstationarity of field dynamics. Here, we establish a criterion for electrode spacing based on the expected accuracy of predicting unsampled field potential from sampled sites. *Approach.* We applied spatial covariance modeling and field prediction techniques based on geospatial kriging to quantify sufficient sampling for thousands of 500 ms μ ECoG snapshots in human, monkey, and rat. We calculated a probably approximately correct (PAC) spacing based on kriging that would be required to predict μ ECoG fields at $\leq 10\%$ error for most cases (95% of observations). *Main results.* Kriging theory accurately explained the competing effects of electrode density and noise on predicting field potential. Across five frequency bands from 4–7 to 75–300 Hz, PAC spacing was sub-millimeter for auditory cortex in anesthetized and awake rats, and posterior superior temporal gyrus in anesthetized human. At 75–300 Hz, sub-millimeter PAC spacing was required in all species and cortical areas. *Significance.* PAC spacing accounted for the effect of signal-to-noise on prediction quality and was sensitive to the full distribution of non-stationary covariance states. Our results show that μ ECoG arrays should sample at sub-millimeter resolution for applications in diverse cortical areas and for noise resilience.

1. Introduction

Electrocorticography (ECoG) is an intracranial electrophysiology tool often used clinically in neurosurgery following innovations in epilepsy treatment by Jasper and Penfield in the late 1940s [1]. The

high signal amplitude and spatial precision resulting from direct cortical contact has provided neurophysiologists with an important tool for studying speech and skeletomotor systems [2–9]. The centimeter scale geometry of ECoG grids has been prioritized for clinical usage. However, there is extensive

evidence that sub-centimeter scale electrode arrays (i.e. millimeter scale contact size and spacing) can resolve finer topographical detail [10] and provide better discrimination for sensory input [11, 12], higher order language processing [13–15], and speech and motor output [16–19].

Application of microfabrication technology has introduced a diverse set of sub-millimeter scale research electrode arrays collectively referred to as ‘micro’ ECoG (μ ECoG) [20–27]. μ ECoG arrays are typically produced with thin film polymers and one or more thin layers of conductive material that can fit over the curvature of neocortex with lower rigidity and bending stiffness than traditional silicon or metal microwire electrodes [28, 29]. μ ECoG arrays sample local field potential (LFP) at sub-millimeter intervals, revealing fine-scale sensory topologies consistent with intracortically mapped topologies in rat barrel cortex [30], rat auditory cortex [23, 31, 32], non-human primate (NHP) somatosensory cortex [33], cat visual cortex [34], and rat ocular dominance columns [35]. Improvements in the integration density of headstage and implanted neural amplifiers are expected to enable orders-of-magnitude scaling of μ ECoG sensor counts [27, 36, 37]. However, LFP, including surface potential, is spatially correlated for physical and physiological reasons, leading to the concern that high density sampling is redundant. Thus, the appropriate sampling resolution for μ ECoG remains an open question.

Prior studies linking primary visual cortex multiunit activity (MUA) to intracortical LFP through a Gaussian integration (point-spread) model have suggested Gaussian kernel scales of $\sim 100 \mu\text{m}$, measured via voltage sensitive dye [38], and between $\sim 100 \mu\text{m}$ in layer 4 to $\sim 200\text{--}300 \mu\text{m}$ in layers 5 and 2/3 in electrode recordings [39]. These (planar) integration models suggest that 95% of the sources contributing to the LFP are within a radius of $250\text{--}750 \mu\text{m}$, and that the full width at half maximum of the point-spread function for a source is $230\text{--}700 \mu\text{m}$. Modeling the impact of pairwise correlations on movement decoding from LFP recorded by arrays of microelectrodes suggests decoded performance is maximized with sub-millimeter spaced electrodes [40]. In an anatomically realistic simulation of field potential, the dynamic factor of synaptic input correlation modulated the spatial reach of source contributions between 100 and $1000 \mu\text{m}$ [41, 42].

The spatial reach of cellular sources on the surface potential has been studied using optogenetic methods. Optical stimulation resulted in μ ECoG-recorded potential profiles extending at least 1 mm in rodents and non-human primates [20, 43–45]. The point spread of surface potential has also been inferred by analyzing the spatial bandwidth of μ ECoG signals, with the conclusion that there is little spatial variation in cycle lengths lower than 0.5–0.7 mm

in rat and rabbit, and 1–3 mm in human [46–48]. Recent correlogram studies that indexed pairwise correlations (or frequency-resolved coherence) by electrode distance suggest that the length scale of spatial correlation varies from 100 to $1000 \mu\text{s}$ of microns depending on electrode contact (epi- versus subdural) and brain state (anesthetized versus awake) [23], and is also highly dependent on the frequency band in question [49–51].

Results regarding characteristic length scales and spatial bandwidth have suggested spatial intervals at which field potential, on average, is no longer redundant. However, no report has discussed the confounding roles of process nonstationarity and signal to noise ratio (SNR) when interpreting auto-covariance functions, nor tested the efficacy of sampling at suggested length scales. We address these topics by using covariance kernel modeling and spatial prediction in a framework known as ‘kriging’ in geospatial statistics [52, 53], and Gaussian processes more generally [54]. Kriging predicts the expected value of unobserved spatial field values conditional on several observed values, under the assumption that all field values are jointly Normal with spatially dependent covariance. As a statistical predictor, kriging also quantifies uncertainty in terms of the expected mean square error (MSE) of the predicted value.

We used kriging prediction error as the key figure of merit to delineate when μ ECoG spatial fields were sufficiently sampled. Based on analysis of theoretical kriging error, we established the competing roles of SNR and electrode spacing in determining the predictability of spatial field details. By manipulating the covariance model, we proposed sufficient electrode spacings required to predict spatial fields with an expected error of 10% of process variance. We tested the theoretical results *in vivo* with cross-validated analysis of kriging error for anesthetized rat auditory cortex μ ECoG recordings, using electrode arrays that were matched in geometry, but differed in noise levels. The different LFP prediction efficiency for the two arrays confirmed the theoretical trade-off between SNR and electrode spacing, and corresponded to the ability to decode sensory information, as measured by a tone frequency classification analysis. In subsequent results, we analyzed the spatial covariance and kriging error of μ ECoG in multiple bandpasses for awake rat, NHP, and anesthetized humans. Submillimeter electrode spacing was generally required for stable prediction at 10% error, although electrode spacing from 1 to 1.5 mm were sufficient for some human and NHP motor cortex bandpasses. Spacing at $600\text{--}850 \mu\text{m}$ was required in all species and cortical areas at the highest 75–300 Hz frequency band, even when recording noise was set to zero in the kriging model. The projected sufficient sampling based on expected kriging error accounted for the full range of covariance states surveyed in our

datasets. Sufficient sampling for kriging prediction is easily tunable for stricter or looser tolerances in other settings, and can be estimated *a priori* given assumptions about LFP image statistics and measurement quality.

2. Methods

2.1. Electrophysiology

2.1.1. Electrode arrays

We measured epidural μ ECoG fields in rat with two types arrays (figure 1 'Rat Arrays'). One was a passively conducting ('passive') array fabricated with gold conductors in liquid crystal polymer (LCP) insulator, manufactured by Dyconex Micro Systems Technologies (Bassersdorf, Switzerland [55]). The other was a custom fabricated 'active' device with NMOS voltage buffering and multiplexing within the array. Gold electrode pads formed the biotissue interface, and were conductively coupled to back-side electronics via highly doped silicon nanomembranes (p^{++} -Si NM), which also functioned as a biofluid insulation material in chemical bond with the main insulation layer of thermally grown silicon-dioxide (t -SiO₂) [56]. Both devices had electrodes arrayed on an 8×8 grid. The active array had 64 rectangular electrodes of $360 \times 360 \mu\text{m}^2$ with $400 \mu\text{m}$ inter-electrode pitch (one electrode was excluded due to malfunction). The passive array included 61 channels (with 3 corners missing) of $229 \mu\text{m}$ diameter discs with $420 \mu\text{m}$ pitch. Impedance could not be measured for the active arrays as a result of their design, but conductor impedance measured with a test structure was $\sim 450 \text{ k}\Omega$ at 1 kHz [56]. Typical *in-vitro* impedance values at 1 kHz for the passive arrays were 21–36 k Ω interquartile range (IQR). A 244-channel LCP and gold μ ECoG array (also manufactured by Dyconex) was used in the human and NHP recordings. These $229 \mu\text{m}$ disk electrodes were arrayed in a 16×16 grid with $762 \mu\text{m}$ pitch with typical *in vitro* impedance values at 1 kHz of 44–53 k Ω IQR (figure 1 'Human Array').

2.1.2. Acute auditory cortex recordings

All rat procedures were performed in accordance with National Institutes of Health standards and were conducted under a protocol approved by the Duke University Institutional Animal Care and Use Committee. Two female Sprague-Dawley rats weighing 260–280 g were anesthetized with ketamine (80 mg kg⁻¹ intraperitoneal) and dexmedetomidine (0.125 mg kg⁻¹ intraperitoneal), and secured to a custom-built orbital clamp head mount. Craniotomies of approximately $6 \times 6 \text{ mm}^2$ were made over temporal cortex, exposing right hemisphere auditory cortical areas. In acute recordings, active and passive μ ECoG arrays were sequentially implanted epidurally. Primary auditory cortex and anterior auditory field (collectively 'auditory cortex') were

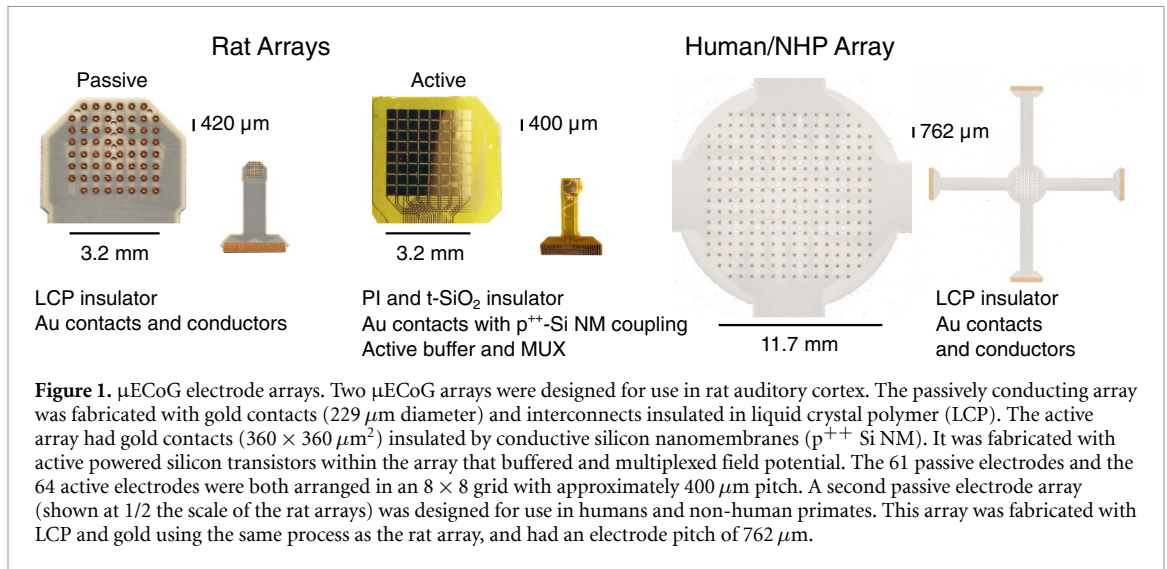
targeted by anatomical landmarks and the reversal of rostrocaudal tonotopic gradients. Neural field potential data from the active array was sampled and logged with a custom National Instruments data acquisition system [57] at an effective rate of 780 S s⁻¹ per channel. Field potential from the passive rat array was amplified and sampled at 20 kS s⁻¹ by an Intan RHD2164 64-channel board with high pass filtering at 0.1 Hz, and logged with the Open Ephys data acquisition system [58].

2.1.3. Chronic auditory cortex implants

Four female Sprague-Dawley rats weighing 225–275 g were anesthetized with 5% isoflurane at 3 l min⁻¹ for induction and 1–3% at 0.5–1.0 l min⁻¹ for maintenance. An identical surgical procedure to the acute preparation was carried out in sterile conditions for placement of passive LCP arrays. Additional procedures regarding surgery and implantation are detailed in [55]. Dexamethasone (0.3 mg kg⁻¹) and Baytril (0.5 mg kg⁻¹) were administered postoperatively for 3 and 7 days respectively. The awake recordings were made with the animals awake and freely moving in their home cages and field potential was acquired in the same manner as acute passive array recordings.

2.1.4. Semi-chronic NHP implant

A semi-chronic recording chamber base was implanted in one adult male NHP (*Macaca mulatta*), as described in [59]. In brief, the NHP was anesthetized during surgical implantation. The base was fixed to the skull with dental cement (MetaBond, Parknell Inc. and Simplex P, Stryker) and ceramic bone screws (Rogue Research). After the chamber base was affixed to the skull, chamber hardware was stacked on top of the base to a height that was tall enough to allow for seal testing of the chamber *in vivo*. After confirmation of chamber seals, a craniotomy and durotomy were performed to provide access to precentral gyrus, and an artificial dura molded with the 244-channel electrode array was implanted within the durotomy. All data collection occurred while the NHP was awake and seated quietly performing a center-out reach task [27]. All animal procedures were performed in accordance with National Institutes of Health standards and were approved by the New York University Animal Welfare Committee (UAWC). Neural data were sampled at 30 kS s⁻¹ (NSpike NDAQ System, Harvard instrumentation Lab, x1 gain headstage, Blackrock Microsystems). Recordings were referenced to a metal screw implanted through the skull to make contact with the dura at a distant location. Of 242 of 244 electrodes that were recorded, we excluded 48 sites that were located across arcuate sulcus in the frontal eye field, and another 11 malfunctioning channels, leaving 183 precentral gyrus sites remaining that covered portions of dorsal premotor cortex and primary motor cortex (collectively 'motor cortex').



2.1.5. Human clinical procedure

Intraoperative recordings were made in two patients (subject A, female, age 20; subject B, female, age 22) undergoing resection surgery in left posterior superior temporal gyrus (pSTG) to treat drug resistant epilepsy. Clinical procedures were performed in accordance with National Institutes of Health standards and were conducted under a protocol approved by the Duke Institutional Review Board. Prior to surgery, each electrode array was pre-selected based on impedance measurements in saline solution. After selection, the electrode array was cleaned and impedance measurements were taken again in saline. The electrode array, electrode holder, and all cables were gas sterilized prior to use in the operating room. In the operating room, patients underwent general anesthesia with propofol (240 mg subject A, 150 mg subject B). Prior to resection, the surgeon placed the 244-channel μECoG electrode (either bare or molded in silicone) to record areas adjacent to the seizure onset zone. Recordings were made in pSTG for subject A (15 min) and motor cortex for subject B (6 min) during acoustic stimulation with words and non-words in vowel-consonant-vowel and consonant-vowel-consonant patterns. Neural responses were amplified and sampled at 20 kS s⁻¹ using four Intan RHD2164 amplifiers held by a 3D printed mount and acquired through Open Ephys software.

2.2. Covariance modeling and kriging prediction

We modeled the μECoG signal $x(s, \tau)$, measured at location s and moment τ , as the sum of a spatially correlated neural field process η (variance $\lambda \mu\text{V}^2$), uncorrelated measurement error ε ($\sigma_n \mu\text{V}^2$), and a common spatial mode κ , which may be zero. Field covariance was estimated using the semivariogram (or variogram) which is half the variance of the difference in signal measured at two locations:

$$\gamma_x(s, u) = \frac{1}{2} \text{var}\{x_s - x_u\}. \quad (1)$$

Due to finite signal energy and compact fields of view, we made the common simplifying assumption of spatially isotropic second-order stationarity, which reduces the variogram to a function of relative distance $h = \|s - u\|$. We also assumed approximate process stationarity over short time windows, to estimate variances over time samples. Under these conditions, we link a field-plus-noise covariance model $C_x(h) = C_\eta(h) + \sigma_n \delta(h)$ to the variogram:

$$\gamma_x(h) = \underbrace{C_\eta(0) - C_\eta(h)}_{\text{neural field}} + \underbrace{\sigma_n(1 - \delta(h))}_{\text{noise}}. \quad (2)$$

We fit empirical variograms with a combination of a constant offset for noise (the ‘nugget’, per spatial statistics literature [60]) and the Matérn kernel [61] for the neural field covariance term. The Matérn kernel is parameterized by a length θ that scales the correlation range, and a unit-less shape parameter ν influences the smoothness of the field at short range. We summarized the noise-free spatial scale of neural fields with the Nyquist pitch, which is the sample spacing that would enable perfect interpolation for bandlimited fields that are sampled with exact precision. We defined the effective Nyquist pitch as the reciprocal of the -30 dB bandwidth of the spatial power spectral density ($\Delta_{\text{nyq}} = BW^{-1}$), calculated via the Fourier transform of the Matérn kernel. This interval corresponded to half of the smallest effective cycle length for a field process. See the supplemental discussion (available online at stacks.iop.org/JNE/18/036011/mmedia) for extended details of the covariance and power spectrum models.

Once a covariance model was estimated, we could derive kriging predictions and errors for the μECoG field. Given a vector of μECoG measurements at n electrodes, $x = (x_1, \dots, x_n)^T$, the kriging predictor of a target site s' is a linear predictor $\hat{\eta}_{s'} = w_{s'}^T x$ that is

optimized for error variance, conditioned on the spatial kernel model. The prediction error variance:

$$\begin{aligned}\sigma_e(s') &= E\{(\eta_{s'} - \hat{\eta}_{s'})^2\} \\ &= \lambda - 2w_{s'}^T \text{cov}\{x\eta_{s'}\} + w_{s'}^T C_x w_{s'},\end{aligned}$$

is minimized by the filter $w_{s'} = C_x^{-1} \text{cov}\{x\eta_{s'}\}$. Noting that the field and noise components of x are uncorrelated, the cross-covariance vector is computed from the neural field kernel absent the nugget $c(s') = (C_\eta(\|s_1 - s'\|), \dots, C_\eta(\|s_n - s'\|))^T$. The kriging predictor is a weighted sum of the sample data with coefficients that depend only on the covariance kernel:

$$\hat{\eta}_{s'} = c(s')^T C_x^{-1} x. \quad (3)$$

Similarly, the prediction MSE depends only on the covariance model and not directly on the data sample itself:

$$\sigma_e(s') = \lambda - c(s')^T C_x^{-1} c(s') \quad (4)$$

The ‘simple’ kriging predictor is the best unbiased linear predictor (BLUP) for a zero mean field. However, the presence of a spatial common mode does not affect the variogram modeling, and can be accommodated in the kriging predictor by constraining $w_{s'}$ to sum to one. The ‘ordinary’ kriging weights are an unbiased predictor of an unknown field value plus a constant mean, and the error has the standard form $\sigma_e(s') = \lambda - 2w_{s'}^T c(s') + w_{s'}^T C_x w_{s'}$ [53]. We used the ordinary kriging predictor for awake recordings, which tended to have more strongly correlated fields. We saw no justification for modeling spatially varying deterministic trends.

2.3. Cross-validated kriging

We quantified kriging error and critical sample spacing by modeling the covariance of μECoG field potential in short-time (500 ms) batches, to better approximate statistical stationarity on a per-batch basis. Empirical variogram clouds were computed from the sample variance of all pairwise electrode differences (figures 2(a and b)), and signal and shape parameters $\{\lambda, \sigma_n\} \cup \{\theta, \nu\}$ of the Matérn-plus-nugget model (equation (2)) were estimated via non-linear least squares fit to binned semivariance medians, weighted by bin count. Total signal variance $\zeta = \lambda + \sigma_n$ (the ‘sill’, per spatial statistics) was constrained to be within $\pm 25\%$ of the total signal sample variance. To account for a common mode variance, which is poorly estimated with the mean of correlated samples, total variance was computed after re-referencing the signal batch to the channel with minimum Euclidean distance to the channel average. Noise power was determined based on heuristic singular value thresholding [62]. Batches with poorly fit covariance were identified by smoothness values

within 0.1 of the $0.3 < \nu < 5$ bounds, and were discarded.

Model prediction errors (equation (4)) were cross-validated with residual errors from kriged μECoG fields, which were made by subsampling half of the array rows and columns and predicting interior sites (avoiding extrapolation, figure 2(c)). With this scheme, four sets of overlapping predictions could be made. The MSE of cross-validated residuals was computed using a 0.5% trimmed mean of square errors, which was robust to heavy-tail outliers [63]. Since the total cross-validated residual MSE included the noise variance of the reference sites, which was independent of the prediction error, we adjusted the total expected MSE to include estimated noise:

$$E\{|\hat{\eta}_{s'} - (\eta_{s'} + \epsilon_{s'})|^2\} = \sigma_e + \sigma_n. \quad (5)$$

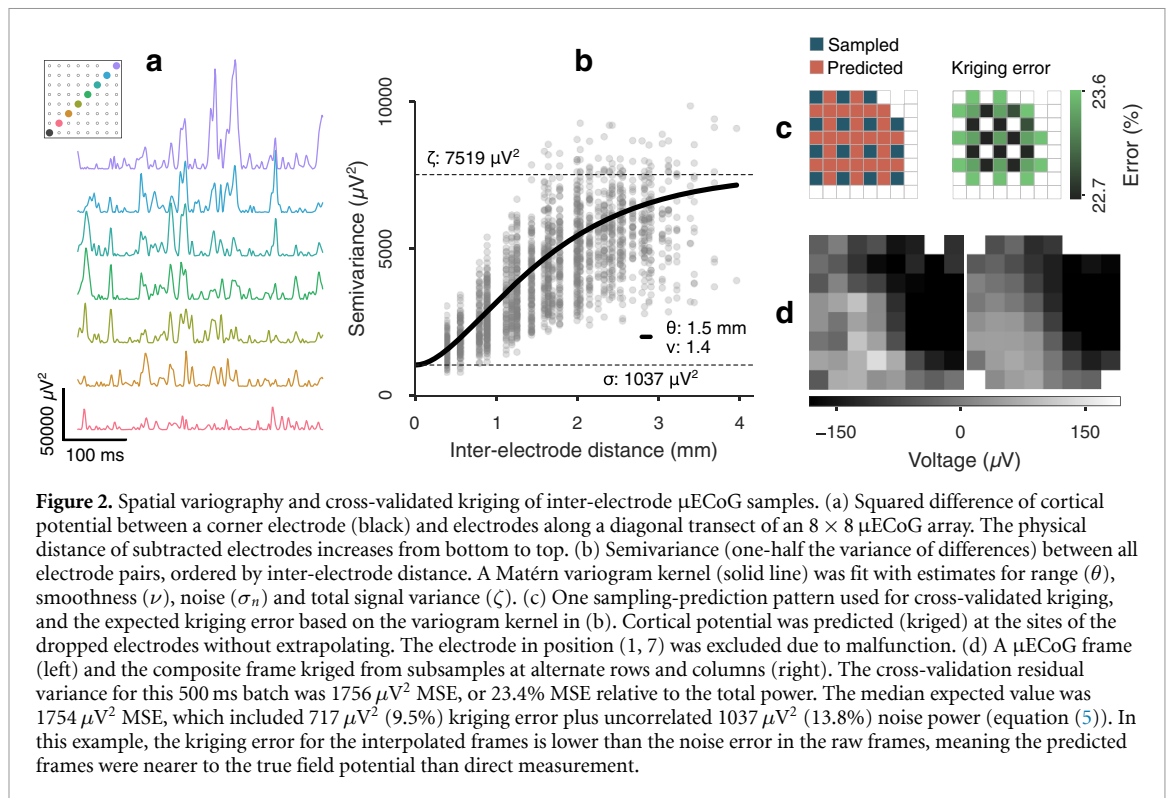
The expected error was calculated per batch for all kriged sites and summarized by the median (figure 2(c)).

We used the Bhattacharyya coefficient (BC) to measure overlap of covariance parameter distributions on a 0–1 scale. Samples were histogrammed into density-normalized bins $\{P_i\}$ and $\{Q_i\}$ using the Freedman Diaconis rule and BC was calculated as $\sum_i (P_i Q_i)^{1/2}$. To find the hypothetical electrode spacing that would result in 10% kriging error—termed the ‘kriging resolution’—we computed $\Delta_{10\%} = \arg \min_{\Delta} |\sigma_e - 0.1|$ via line-search along inter-electrode pitch Δ while holding the covariance kernel parameters $\{\theta, \nu, \sigma_n/\zeta\}$ constant in equation (4).

2.3.1. Signal bandpasses

All recordings (except from the active array) were anti-alias filtered offline at 800 Hz and then resampled at 2 kSs^{-1} . We applied cross-validated kriging analysis to multiple commonly defined LFP frequency bands. We used approximately log-spaced frequency bands (following [50]): theta (4–7 Hz), alpha (7–14 Hz), beta (15–30 Hz), and gamma (30–60 Hz). Additionally, we used a wide high frequency broadband (HFB) (75–300 Hz) in which power modulation has been linked to neuronal spiking rates [64, 65], and which includes high gamma (roughly 80–200 Hz) that is used for measuring stimulus- and behavior-related activity in human ECoG [2–6]. While broadband power fluctuations are technically a full-spectrum phenomenon, we use ‘HFB’ to denote a bandpass generally free of narrow-band oscillatory activity [66].

A 4–300 Hz band was used to summarize the union of these frequency bands. However, due to the elevated transistor noise of the ‘active’ electrode array, kriging analysis for the acute rat auditory cortex recordings was restricted to 5–100 Hz.



2.4. Tone stimulation and classification

Acute rat auditory cortex recordings were carried out in a sound-attenuated chamber. We played 60 repeats of tone pips for 13 frequencies (0.5–32 kHz, 0.5 octave spacing, 50 ms duration, 2 ms cosine-square ramps) at a rate of 1 s^{-1} in pseudorandom sequence (780 trials). Acoustic stimuli were generated with custom MATLAB code through an NI 6289 DAC card, and delivered at 70 dB SPL through a free-field speaker (CR3, Mackie) calibrated to have a flat output over the frequency range used.

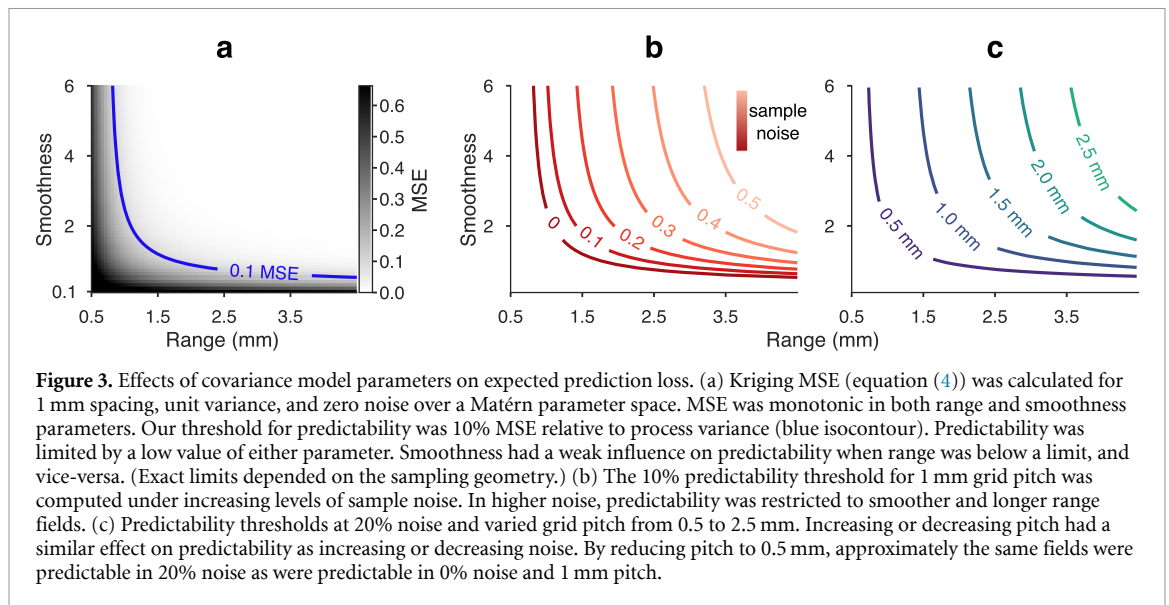
We analyzed the effect of electrode spacing on predicting auditory stimuli using a previously reported principal components analysis (PCA) and linear discriminants analysis (LDA) classification scheme [32, 55]. To vary electrode spacing in a continuous manner, we used Poisson Disc sampling [67] to generate subsets of the passive rat array that were approximately periodic in space: 10 subsets for spatial periods between 420 and 2000 μm in 25 μm steps. The effective inter-electrode distance was calculated as the square root of area per electrode: $\Delta = (A/n)^{1/2}$, where A was derived by the electrode set's convex hull (see figure 6(a)). The concatenated response from 50 ms post-stimulus μECoG on subset channels was used to form feature vector, and the SVD thresholding heuristic used for noise estimation [62] was used to determine the number of feature PCs to use in the LDA stage. Six-fold cross-validation was then used to produce tone frequency predictions for each trial.

3. Results

3.1. Theoretical and *in vivo* analysis of sampling noise and density

The proposed electrode spacing requirements based on prediction loss followed from analytical results of kriging theory, which we outline here. We noted that optimal prediction loss (equation (4)) was a function of (a) the length-scale and texture qualities of a spatial field, (b) the SNR of the measurements, and (c) the electrode array geometry vis-a-vis the location to be predicted. Since the expected loss was completely parameterized by the covariance model, we could compute results *a priori* in response to the three relevant geospatial and signal factors.

Using the Matérn covariance model (equation (2)) with unit variance and zero noise, we calculated kriging errors on a 10×10 grid geometry with 1 mm pitch over a range of length scale and smoothness parameters (figure 3(a)). Error approached high levels ($>50\%$ of process variance) for fine-scale models having short range and low smoothness, and was particularly affected by rough texture (low smoothness) fields at all length scales. Such rough spatial fields would be highly irregular within short-distance neighborhoods, regardless of the dominant spatial length scale indicated by θ . Error was monotonic with both spatial parameters, and we defined an error of 10% MSE relative to process variance (0.1 relMSE) to partition the range of covariance models into predictable and not-predictable subsets. The 1 mm pitch



in this geometry implied that the covariance models along the predictability threshold had a $\Delta_{10\%}$ ‘kriging resolution’ of 1 mm.

We then repeated the prediction MSE calculations while introducing noise in the covariance kernel. Figure 3(b) depicts the predictability thresholds for noise levels at 10% increments overlaid in Matérn parameter space. The subset of predictable models at 1 mm spacing (equivalent to panel (a) at 0% noise) became increasingly lower resolution (smoother and longer range) with higher noise. In other words, 1 mm spacing had the same prediction efficiency for a finely featured (high resolution) field in low noise and a coarsely featured (low resolution) field in high noise.

We next explored how sample spacing affected the coverage of predictable models. Holding noise at 20%, we calculated prediction MSE for a 10×10 grid arrangement with electrode pitch in 0.5 mm increments. Predictability thresholds for all spacings are overlaid in figure 3(c). Comparing figures 3(b) and (c), increased noise and increased density (larger pitch) moved the predictability threshold in competing directions, such that the loss of coverage in higher noise was almost directly counteracted by higher density. Approximately the same subset of field models predictable at 10% MSE or lower in noiseless conditions was predictable in 20% noise by reducing electrode spacing from 1 to 0.5 mm.

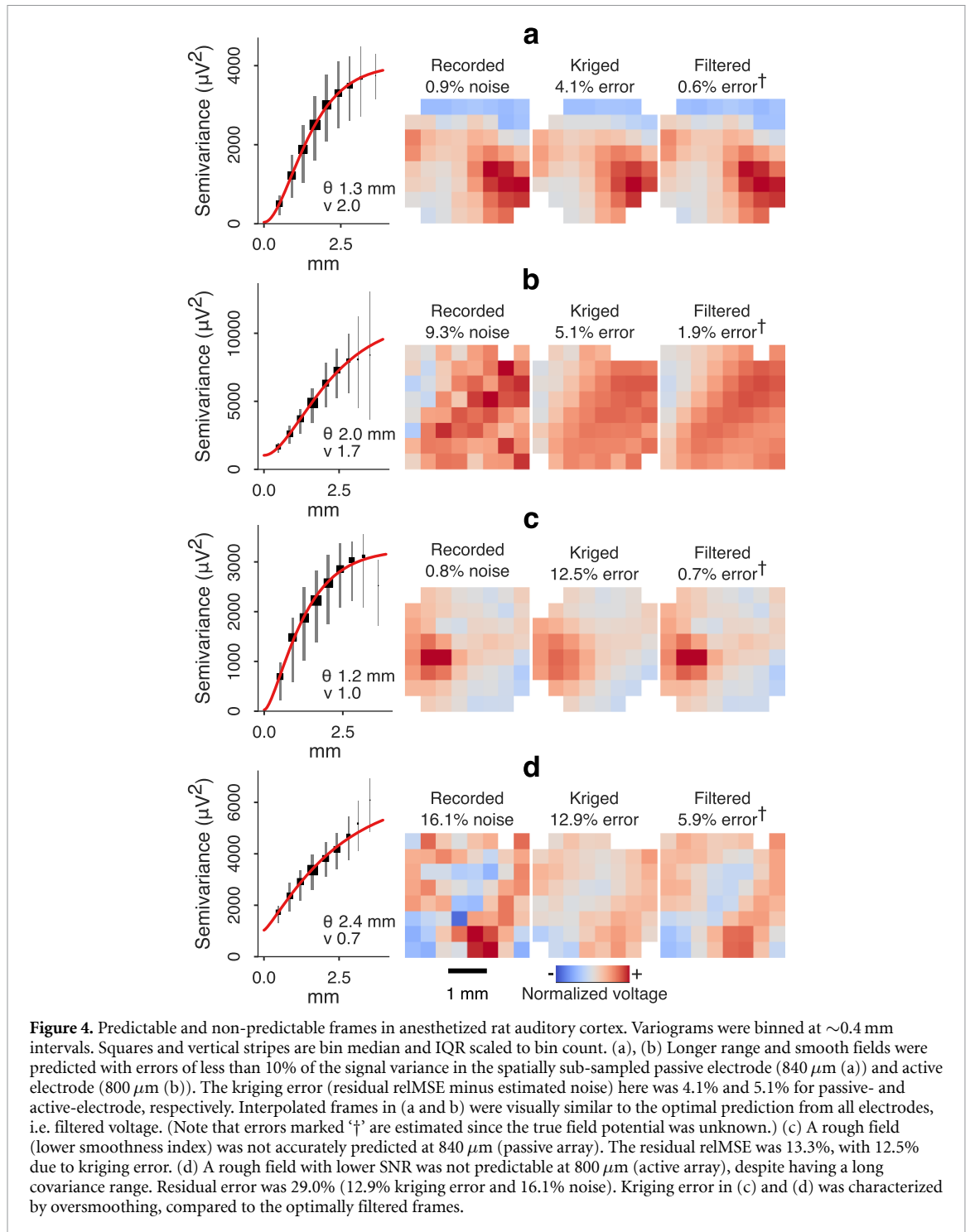
We confirmed the theoretical effects of covariance model parameters on cross-validated prediction errors made from four paired epidural μ ECoG recordings of auditory cortex in two rats, using ‘active’ and ‘passive’ arrays that had similar geometry but different noise properties. Covariance modeling and kriging were carried out on 6540 (3459 active and 3081 passive) short-time 500 ms batches of signal in the 5–100 Hz bandpass (outlined in figure 2 and section 2.3). Extensive evaluation of kriging prediction with *in vivo* μ ECoG and simulated noise can

be found in supplemental materials (supplemental figure S3).

The spatial field and measurement signal statistics highlighted in the previous section accurately delineated predictable versus non-predictable μ ECoG batches. See figure 4 and supplemental videos S1–S4 for specific examples. In aggregate, the expected kriging errors based on covariance models were highly consistent with cross-validated kriging prediction errors. Ordinary least squares (OLS) regression of expected error (equation (5)) from observed relMSE, normalized by the sill variance, resulted in slopes of 0.99 and 0.98 for active and passive batches, respectively ($r^2 = 0.989$, combined model using slopes only).

The covariance model parameters illustrated the distinction between ‘field’ and ‘signal’ properties of the two arrays (figures 5(a) and (c)). Statistics corresponding to the neural potential field, i.e. correlation range, smoothness, and field variance, were largely overlapping (smoothness BC = 0.99; range BC = 0.95; noise-compensated field variance BC = 0.98). The larger covariance range estimated for the active array (1.65 mm median) versus passive array (1.38 mm median) may be explained by shorter edge-to-edge distances in the active array, which were $140 \mu\text{m}$ less than that of the passive array, and would likely increase correlation and bias the Matérn length scale.

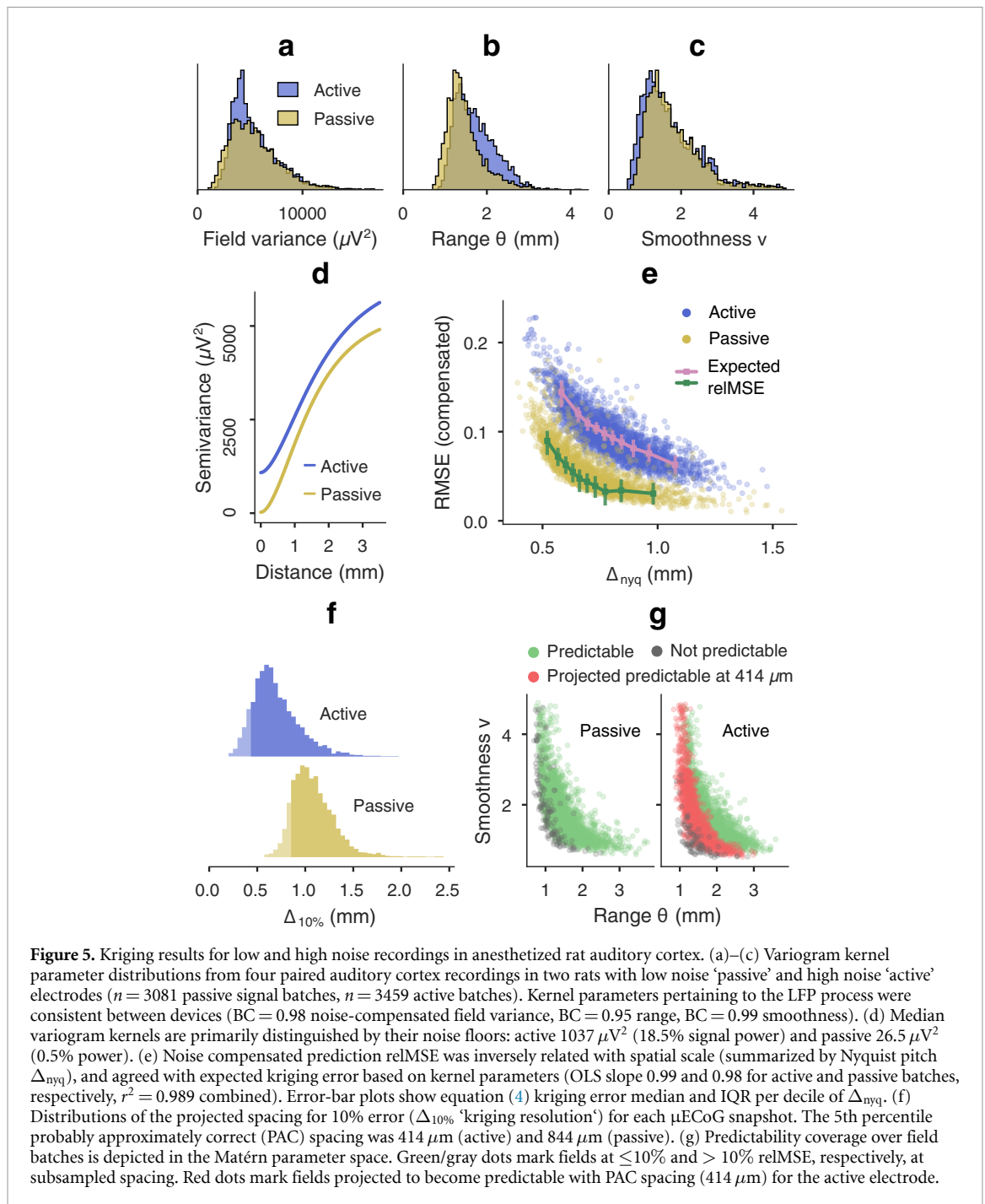
The buffering and multiplexing transistors in active arrays introduce $1/f$ and aliased wideband noise [27]. Median noise estimated by SVD [62] was $1037 \mu\text{V}^2$ for the active array used here, which agreed with bench-top measurements of $992 \pm 308 \mu\text{V}^2$ (mean \pm SD, 5–100 Hz). The noise level was also consistent with the $870 \mu\text{V}^2$ difference in median sill variance between active array and passive array batches. The separability of field and signal qualities was summarized by the average variograms for



each device, which differ mainly by the vertical offset representing the noise floor of the active array (figure 5(d)).

Figure 5(e) depicts the inverse relationship between the Nyquist pitch Δ_{nyq} , and the noise-compensated prediction relMSE that is attributed to kriging prediction error. The increased error for smaller pitches echoed the tendency towards higher error for smaller model parameters in figure 3(a). Increased noise in the active array resulted in uniformly higher compensated relMSE, which shifted the 10% relMSE threshold to lower resolution fields,

as in figure 3(b). Figure 5(e) also shows the extent to which imperfect measurement and lack of band-limiting prevented lossless interpolation even when the subsampled electrode spacing was equal to or less than the effective Nyquist pitch. However, the prediction relMSE for active array fields (median 9.3%) was lower than the noise error (median 18.5%) in 3290/3459 (95.1%) of field snapshots, indicating that the interpolated fields were a better approximation of true cortical potential than the original measurements. We further validated denoising results for interpolated and *in situ* field prediction using



controlled amounts of additive Gaussian white noise, summarized in supplemental figures S3–S4.

We computed the empirical predictability ‘coverage’, at 0.1 compensated relMSE, for the two subsampled μECoG arrays. 95.2% of passive array snapshots were predictable at $840 \mu\text{m}$, compared to 33.0% of active array snapshots at $800 \mu\text{m}$. By manipulating the electrode spacing term in equation (4), we calculated the kriging resolution ($\Delta_{10\%}$) that would normalize prediction error to 10% MSE for each μECoG batch (figure 5(f)). Due to the competing roles of electrode spacing and SNR, shorter electrode spacings would be needed for stable interpolation from active array measurements.

To concisely summarize uncertainty in both the range of model statistics and kriging prediction quality, we adopted the terminology probably approximately correct to specify a single target for electrode spacing and prediction error (loosely based on the rigorous PAC learning theory, see [68] for a definition). For potential fields recorded with very low noise in anesthetized, epidural rat auditory cortex, $840 \mu\text{m}$ electrode spacing had a high probability ($\sim 95\%$ empirical rate) of enabling approximately correct ($\leq 10\%$ error) prediction of unseen field potential. However, the 95%–10% PAC electrode spacing for the same potential fields in a high noise scenario was projected at $414 \mu\text{m}$, based on the

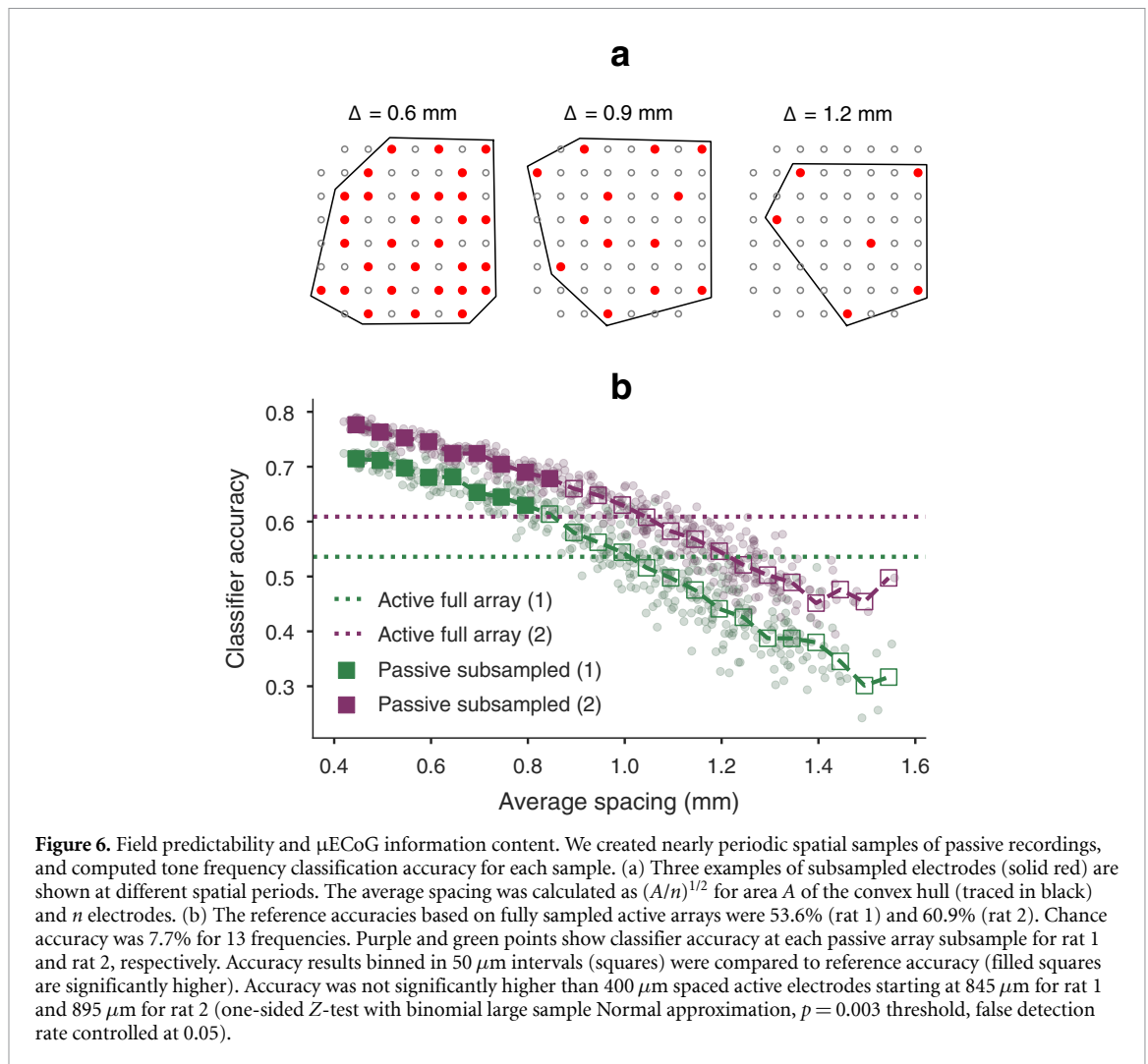


Figure 6. Field predictability and μ ECoG information content. We created nearly periodic spatial samples of passive recordings, and computed tone frequency classification accuracy for each sample. (a) Three examples of subsampled electrodes (solid red) are shown at different spatial periods. The average spacing was calculated as $(A/n)^{1/2}$ for area A of the convex hull (traced in black) and n electrodes. (b) The reference accuracies based on fully sampled active arrays were 53.6% (rat 1) and 60.9% (rat 2). Chance accuracy was 7.7% for 13 frequencies. Purple and green points show classifier accuracy at each passive array subsample for rat 1 and rat 2, respectively. Accuracy results binned in $50 \mu\text{m}$ intervals (squares) were compared to reference accuracy (filled squares are significantly higher). Accuracy was not significantly higher than $400 \mu\text{m}$ spaced active electrodes starting at $845 \mu\text{m}$ for rat 1 and $895 \mu\text{m}$ for rat 2 (one-sided Z -test with binomial large sample Normal approximation, $p = 0.003$ threshold, false detection rate controlled at 0.05).

5th percentile of $\Delta_{10\%}$ in active array batches. The projected expansion of predictability coverage from 800 to $414 \mu\text{m}$ is shown in figure 5(g), echoing the recovery of predictability in the simulated results in figure 3(c).

3.2. Field predictability and stimulus information content

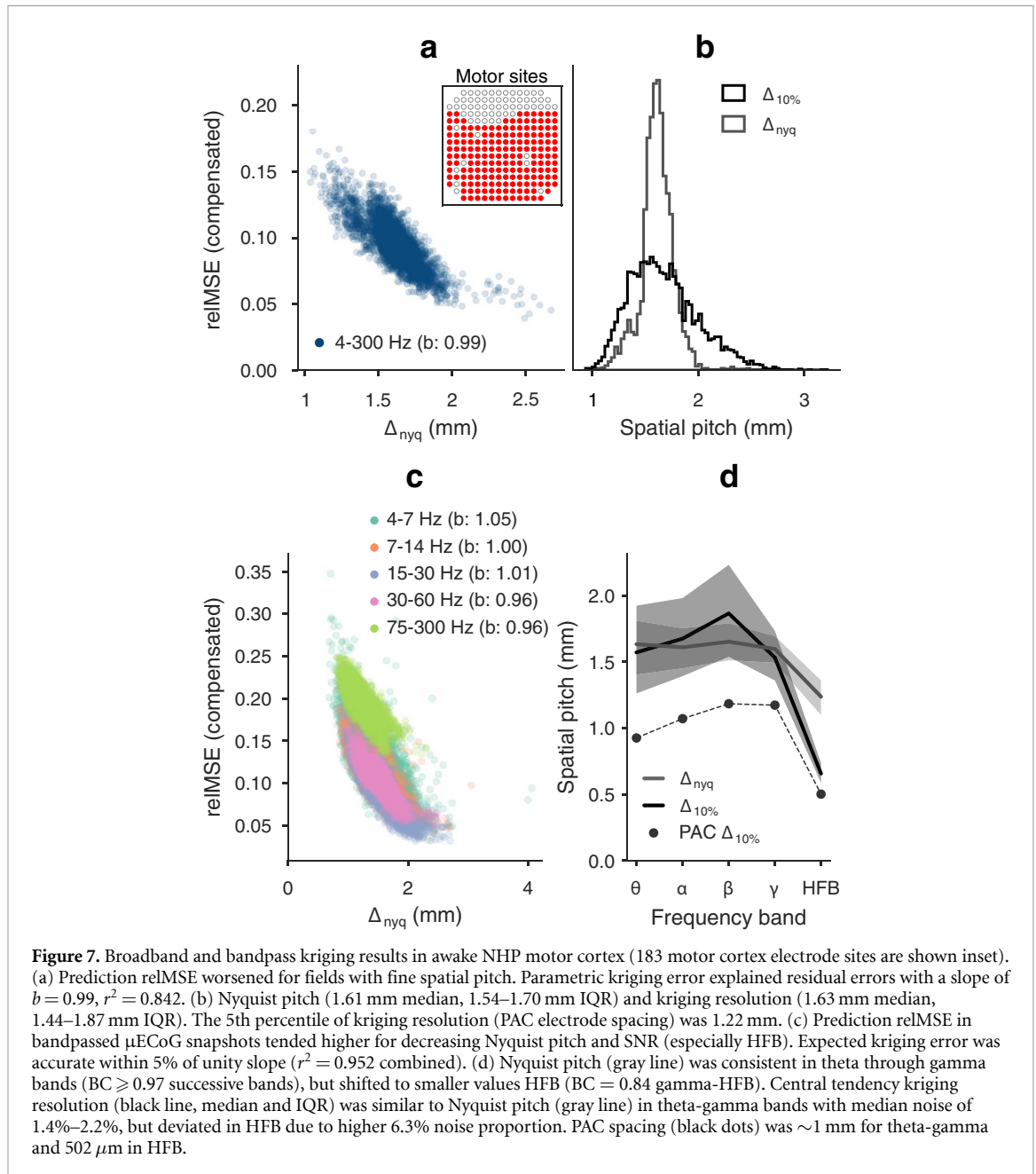
We have observed previously [27] that, despite similar electrode geometry and recording conditions, auditory stimulus classification accuracy is lower using active array recordings compared to passive, due to increased noise. Here we used tone classification to test whether the hypothetical equivalence in active- and passive array sampling predictability corresponded to equivalent information content in the signals. We gradually reduced the effective inter-electrode distance of the passive array from $420 \mu\text{m}$ to $\sim 2000 \mu\text{m}$ to compare classifier accuracy with that from active arrays sampled at $400 \mu\text{m}$ (53.6% for rat 1 and 60.9% for rat 2, figure 6).

As expected, passive array classifier accuracy at full sampling (72.4% for rat 1 and 78.2% for rat 2) outperformed corresponding active arrays, and

decreased fairly regularly as fields were sampled more sparsely. To determine where the subsampled accuracy rates intersected with the corresponding active array baselines, we binned results at every $50 \mu\text{m}$ and used the large-sample Normal approximation (with $\sigma^2 = p(1-p)/780$) to calculate z-scored accuracy differences. The smallest electrode spacing bin with no significant difference in accuracy rates was $845 \mu\text{m}$ for rat 1 and $895 \mu\text{m}$ for rat 2 (one-sided Z -test, $p < 0.003$ with false detection rate controlled at 0.05). The equivalent spacing for stimulus information content agreed the hypothesized equivalent PAC spacings of 840 and $414 \mu\text{m}$.

3.3. Kriging resolution in rat, NHP, and human μ ECoG

We analyzed spatial covariance in multiple band-passes for μ ECoG recordings from one semi-chronically implanted NHP performing a center-out reach task, two intra-operatively implanted humans listening to word/non-word acoustic stimulation under anesthesia, and four chronically implanted rats listening to tone pips while awake and freely moving. We used four commonly defined oscillatory



bandpasses (theta: 4–7 Hz, alpha: 7–14 Hz, beta: 15–30 Hz, gamma: 30–60 Hz) and a high frequency broadband (75–300 Hz) characterized by wide spectrum power fluctuations.

3.3.1. NHP motor cortex

We recorded neural potentials from 183 of 244 electrodes with 762 mm pitch in motor cortex of a macaque performing a center-out reach task (figure 7(a) inset). Bandpassed and broadband spatial variance modeling of 4161 500 ms batches accurately predicted cross validated kriging error, with $b = 0.99$ in broadband signal and $0.96 < b < 1.05$ among bandpasses. There was a lower degree of precision in the expected model error for broadband signal ($r^2 = 0.842$) versus bandpasses ($r^2 = 0.952$).

Broadband fields in awake NHP motor cortex had longer correlation range and rougher texture compared to anesthetized rat auditory cortex, with median $\Delta_{nyq} = 1.61$ mm. The larger subsampled electrode spacing of 1.52 mm predicted 62.3% of field batches at 10% MSE or lower. The hypothetical kriging resolution for 95%–10% PAC coverage was 1.22 mm. At 2.1% median noise, the PAC sample spacing compared closely to the same 5% quantile of Nyquist pitch, which was 1.33 mm (figures 7(a) and (b)).

The spatial properties of bandpassed μ ECoG fields from theta to gamma were extremely consistent (note the overlapping sets in figure 7(c)). The Nyquist pitch distributions from theta to gamma (pairwise $BC \geq 0.91$) had median values highly consistent with the broadband 1.6 mm median. Noise was also similar

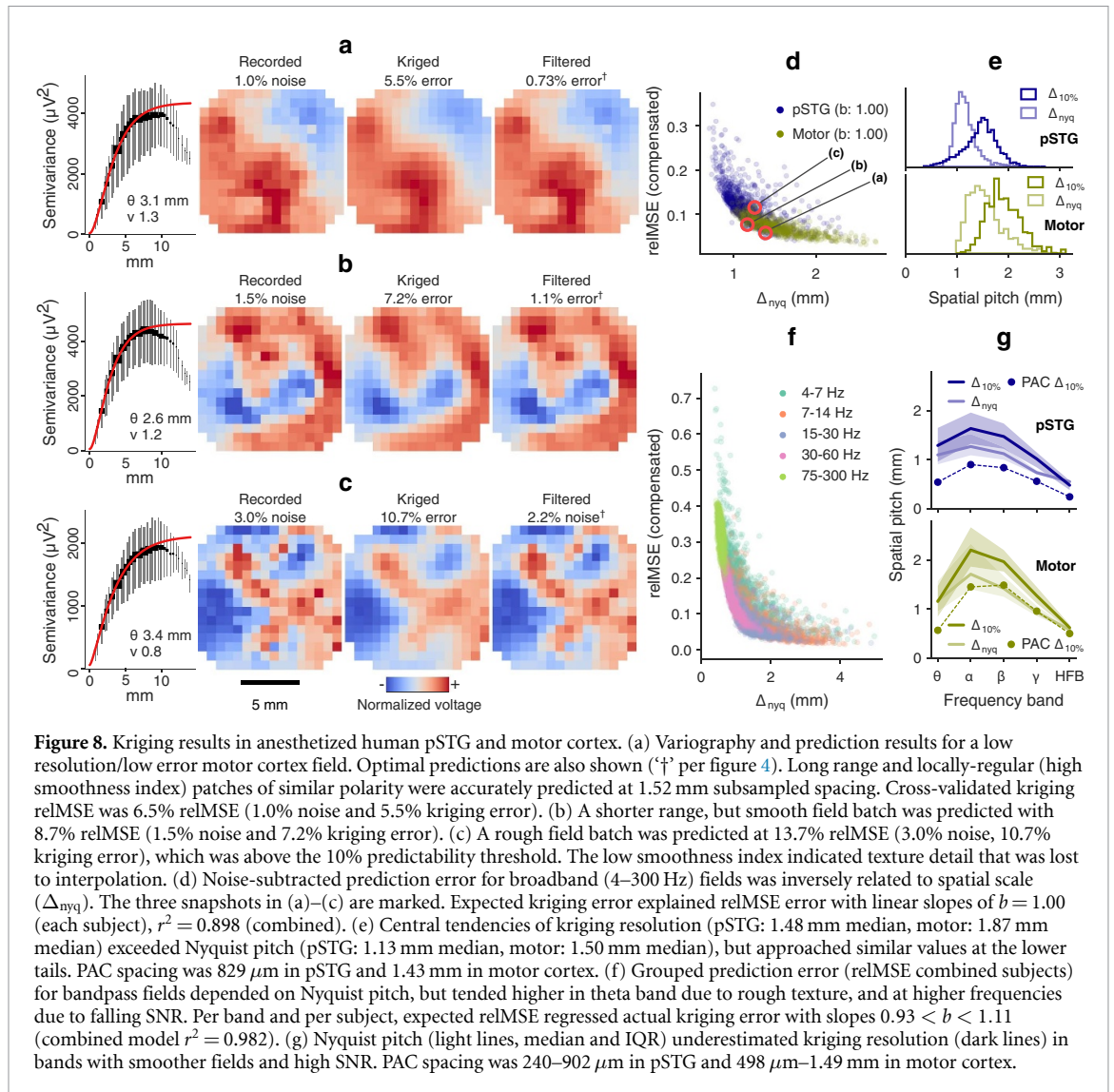


Figure 8. Kriging results in anesthetized human pSTG and motor cortex. (a) Variography and prediction results for a low resolution/low error motor cortex field. Optimal predictions are also shown (\dagger per figure 4). Long range and locally-regular (high smoothness index) patches of similar polarity were accurately predicted at 1.52 mm subsampled spacing. Cross-validated kriging relMSE was 6.5% relMSE (1.0% noise and 5.5% kriging error). (b) A shorter range, but smooth field batch was predicted with 8.7% relMSE (1.5% noise and 7.2% kriging error). (c) A rough field batch was predicted at 13.7% relMSE (3.0% noise, 10.7% kriging error), which was above the 10% predictability threshold. The low smoothness index indicated texture detail that was lost to interpolation. (d) Noise-subtracted prediction error for broadband (4–300 Hz) fields was inversely related to spatial scale (Δ_{nyq}). The three snapshots in (a)–(c) are marked. Expected kriging error explained relMSE error with linear slopes of $b = 1.00$ (each subject), $r^2 = 0.898$ (combined). (e) Central tendencies of kriging resolution (pSTG: 1.48 mm median, motor: 1.87 mm median) exceeded Nyquist pitch (pSTG: 1.13 mm median, motor: 1.50 mm median), but approached similar values at the lower tails. PAC spacing was 829 μm in pSTG and 1.43 mm in motor cortex. (f) Grouped prediction error (relMSE combined subjects) for bandpass fields depended on Nyquist pitch, but tended higher in theta band due to rough texture, and at higher frequencies due to falling SNR. Per band and per subject, expected relMSE regressed actual kriging error with slopes $0.93 < b < 1.11$ (combined model $r^2 = 0.982$). (g) Nyquist pitch (light lines, median and IQR) underestimated kriging resolution (dark lines) in bands with smoother fields and high SNR. PAC spacing was 240–902 μm in pSTG and 498 μm –1.49 mm in motor cortex.

at 1.4%–2.2% levels, but the actual 10% MSE predictability coverage at 1.52 mm was higher for alpha and beta bands (77.0% and 74.6%, respectively) than for theta and gamma (41.1% and 55.9%, respectively). PAC sample spacing was 0.93–1.18 mm in the theta to gamma bandpasses (figure 7(d)).

The combination of finer spatial scale (median $\Delta_{nyq} = 1.24$ mm) and higher noise (median 6.3%) in HFB had a significant impact on kriging prediction error. The minimum compensated relMSE was 12.4%, meaning there was no predictability coverage at the 1.52 mm electrode spacing. We projected the 95%–10% PAC to be 502 μm in the HFB bandpass.

3.3.2. Human pSTG and motor cortex

We applied the kriging experiment to μECoG recorded from motor cortex in two human volunteers undergoing surgery for drug resistant epilepsy. The 244-channel electrode was implanted intraoperatively and field potential was recorded outside the seizure onset zone while subjects were anesthetized.

Recordings were split into short-time batches (1560 subject A pSTG, 662 subject B motor). Model-based expected error was generally accurate explaining cross-validated kriging error for broadband ($b = 1.00$ for both subjects) and bandpassed fields ($0.95 < b < 1.11$ subject A, $0.92 < b < 1.03$ subject B), with a difference in precision as noted in NHP fields (broadband $r^2 = 0.898$, bandpass $r^2 = 0.982$, combined factors models).

Examples of 4–300 Hz broadband fields from subject B with three different covariance characteristics are shown in figure 8(a)–(c) (and in animated form in supplemental videos S5–S7). The most predictable fields were those with smooth texture and large extents of equal polarity (e.g. figure 8(a)). As indicated by the analytical results, texture strongly affected the error of kriging predictors. Two field batches in figures 8(b) and (c) had dominant spatial cycle limits (Δ_{nyq}) of 1.16 and 1.25 mm, respectively, less than the subsampled pitch of 1.52 mm. However, the smoother texture in figure 8(b) led to recovery at 7.2% MSE, while more granular features in

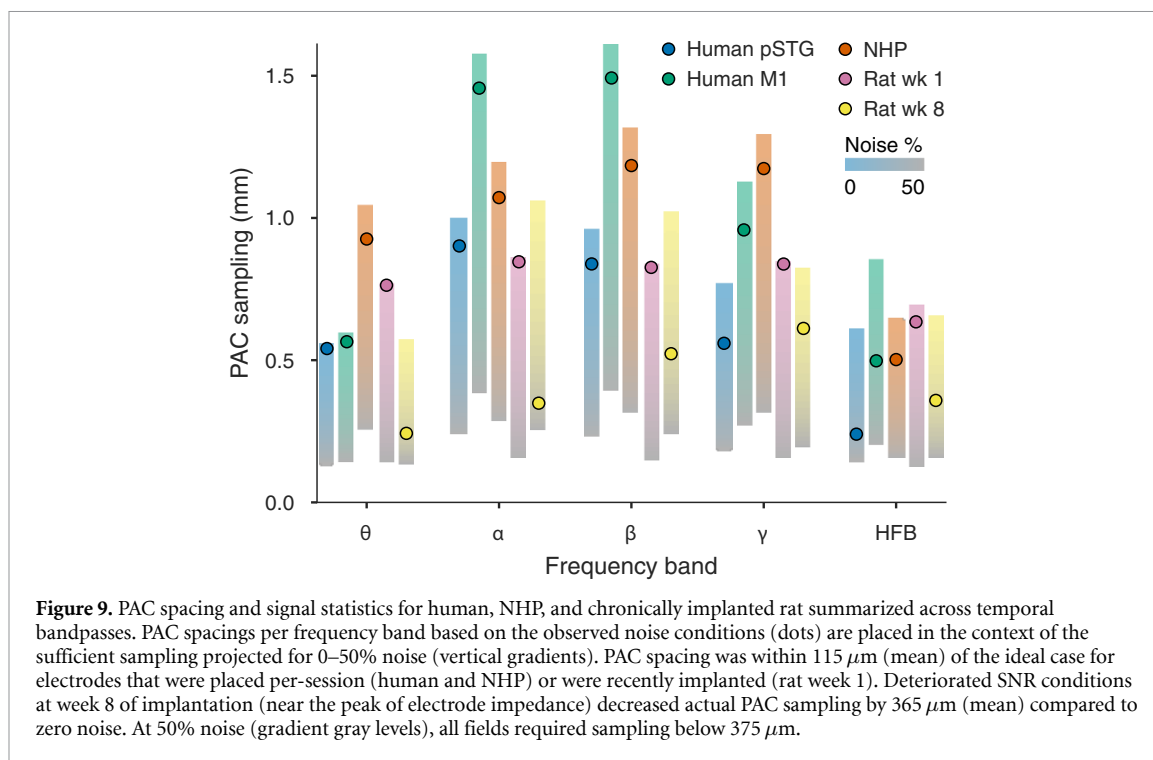


figure 8(c) were considered ‘not predictable,’ at 10.7% MSE. In figure 8(a)–(c), the divergence of the empirical semivariogram from an asymptotic variance at long range is likely due to these points being the least reliable estimates of semivariance [69]. These points were down-weighted in the model fit, as indicated by the visual weight in the figures.

Broadband motor cortex fields were of similar spatial scale in human (median $\Delta_{\text{nyq}} = 1.50$ mm) as in NHP, while pSTG fields were smaller scale (median $\Delta_{\text{nyq}} = 1.13$ mm). The difference in Nyquist pitch corresponded to 91.8% predictability coverage in motor cortex at the actual 1.52 mm electrode spacing, but only 42.7% predictability coverage in pSTG (figure 8(d)). PAC spacings were 1.43 mm and 829 μm respectively (figure 8(e)).

As a group, bandpassed human μECoG fields were predicted less effectively at smaller length scales (figure 8(e)). There was also greater variability between bands in both brain areas, compared to NHP motor cortex. Median Nyquist pitch peaked in the alpha band (1.27 mm, subj. A, 1.72 mm, subj. B), which may have been influenced by a moderate increase of coherent alpha rhythms in temporal areas during general anesthesia under propofol [70]. Median kriging resolution spacings exceeded the subsampled electrode spacing of 1.52 mm in bands with larger Nyquist pitches and lower noise proportions (figure 8(g)). For generally stable prediction, we estimated the PAC spacing in pSTG to be between 902 μm (alpha band) and 240 μm (HFB), and in motor cortex between 1.49 mm (beta band) and 324 μm (HFB). See figure 9 for detailed PAC spacing and noise

results. Supplemental videos S8–S12 show recorded, kriged, and filtered human μECoG snapshots for each bandpass.

3.3.3. Combined effects of spatial scale and noise

To incorporate fields recorded in a chronic implantation setting, we also analyzed spatial field characteristics for a cohort of four rats implanted with the passive electrode array in auditory cortex [55]. We used recordings made in the first week and the eighth week of implantation, at which point the acute tissue response was presumed to have stabilized and electrode impedance was near peak levels.

In figure 9, we summarized the PAC sampling results in rat, NHP, and human in the context of the particular SNR that we observed in those recordings. After manipulating the electrode spacing term for the expected kriging error to find the PAC predictability boundary, we also varied the share of noise in covariance models on the boundary to project PAC spacings for 0–50% noise levels. PAC electrode spacings in the ideal scenario were uniformly submillimeter for HFB fields in all cortical areas and species. Spacings were approximately 1 mm or lower for auditory cortex in rat and pSTG in anesthetized human. Except in HFB and theta bands, motor cortex fields in both NHP and human were projected to be predictable at spacings between ~ 1 and 1.5 mm.

In all cases, the compensatory balance of spatial oversampling in the presence of noise reduced estimation of the 95%–10% PAC spacing. Values for ‘new’ implants (intraoperative human, semi-chronic NHP, and early rat electrodes) were within an average of 115 μm of ideal PAC spacings across bands. However,

anesthetized human fields showed notable deviations from ideal PAC spacings at HFB of $371\ \mu\text{m}$ (pSTG) and $354\ \mu\text{m}$ (motor).

In the chronic implant setting, field statistics were relatively stable between week 1 and week 8, with overlap in Nyquist pitch having mean $BC = 0.90$. By week 8, $1/f$ thermal noise from increased electrode impedance deteriorated signal quality at lower frequencies, raising median noise proportion from 1.2% to 9.2% mean across bands (mean $BC = 0.11$). The signal properties had a significant effect on predictive sampling. At the first week of implantation, very low noise fields could be sampled effectively with $635\text{--}846\ \mu\text{m}$ PAC spacing across bands, similar to results in anesthetized auditory cortex during the same acoustic tone stimulation. The PAC kriging resolution for week 8, as a product of SNR and field resolution, was $243\text{--}612\ \mu\text{m}$, which was lower than ideal by $200\text{--}700\ \mu\text{m}$ ($365\ \mu\text{m}$ mean).

4. Discussion

In the preceding results, we analyzed sufficient spatial sampling of cortical surface potential with the objective of predicting continuous voltage fields with constrained loss of detail. From basic analytical results, we expected that predictability should depend on three independent factors: (a) the natural image statistics of the cortical field potential (the ‘field’), (b) the precision of measuring those potentials (the ‘signal’), and (c) the electrode sampling geometry. In particular, this analysis suggested that prediction loss induced by substantial noise or fine feature scale can be corrected with greater sampling density.

We established through covariance modeling and cross-validated predictions that the theoretically expected kriging error accurately explained prediction MSE across a range of field, signal, and electrode spacing conditions. Next, we extrapolated electrode spacings for each short-time batch that would normalize expected kriging error to 10% of the process variance (although a lower tolerance could be used in practice). Based on the distributions of spatial field statistics in a variety of regimes, we proposed electrode spacings that were ‘probably approximately correct’, i.e. resulting in $\leq 10\%$ approximation error for $\geq 95\%$ of the observed fields. The mathematically rigorous PAC learning framework [68] was only loosely adapted here, but the ‘probable’ and ‘approximate’ concepts succinctly described the task of seeking a sufficient sampling density to constrain loss under non-stationary conditions. In an experiment with controlled neural field statistics and electrode geometry, we found that different μECoG signals sampled at 95%–10% PAC predictability spacings generated approximately equivalent stimulus classification accuracy.

For the fields we observed, PAC sample spacing in ideal (noiseless) conditions was between about $570\text{--}1050\ \mu\text{m}$ across bandpasses for rat auditory cortex. NHP and human motor cortex fields in the alpha, beta, and gamma bands could be predictably sampled in the $1\text{--}1.5\ \text{mm}$ range, while human pSTG fields required sampling at approximately $600\text{--}1000\ \mu\text{m}$. HFB required sampling between 600 and $850\ \mu\text{m}$ for all cortical areas and species, assuming noiseless conditions, while the $4\text{--}7\ \text{Hz}$ theta band also required $\sim 500\ \mu\text{m}$ sampling for human fields and rat fields at week 8, after implants had stabilized. Adjusted to the noise levels we observed, PAC sample spacing was, on average, $115\ \mu\text{m}$ smaller than the ideal case for intraoperative or semi-chronic electrode placements, with the largest deviations occurring in HFB. In the long-term chronic case, increased thermal noise reduced PAC sampling $365\ \mu\text{m}$ on average relative to the noiseless ideal.

Optimal linear combination techniques based on sensor covariance are commonly used for inverse problems in electro- and magnetoencephalography [71–73], and other spatial filters have been proposed to maximize spatial contrast [74]. To the best of our knowledge, this is the first study to rigorously apply optimal linear prediction methods to interpolate field potential based on spatial statistics. While other interpolation methods may yield a similar quality of predictions, a statistical interpolator forecasts the uncertainty of its prediction, i.e. equation (4). The model-based kriging error was the basis of our determination of sufficient sampling, but it also revealed the denoising benefit of correlated sampling. The kriging error for interpolated fields was often smaller than the estimated noise in the original recording. This result indicated that electrode spacing can be tuned for small approximation errors, even below the sensor noise limit, by sufficient oversampling of correlated field potential.

We also made use of *in situ* prediction, as opposed to interpolation, to produce denoised views of neural fields (e.g. figures 8(a)–(c)). Any linear filter (e.g. Gaussian smoothing, spatial averaging, etc) may enhance SNR in a correlated field with spatially independent noise. Kriging produces the best linear unbiased predictor, optimized conditional on the variance model, which tends to perform well compared to deterministic interpolators such as splines or inverse-weighted prediction [75]. Kriging is also *adaptive* to the field statistics, which vary in time. A more thorough analysis of denoising performance based on the approximately noise-free rat auditory field recordings is available in supplemental material (supplemental figures S3 and S4). Since measurement noise may be an unavoidable consequence of electronics miniaturization, intentional spatial oversampling coupled with spatial filtering is a promising strategy to recover high fidelity neural fields. Curves

for hypothetical field coverage vis-a-vis electrode spacing and noise (as in figure 3(a)–(c)) could help guide electrode array design.

Prior investigations of neural signal correlation have made length scale inferences from either the correlogram or its dual, the spatial power spectrum. However, the analyses in these studies were device dependent. Recent results for ECoG in awake humans found electrode spacings at which correlation crossed a threshold of 1/2. One, using a parametric model, revealed length scales in STG ranging from 1.5 mm for gamma and high-gamma to >4 mm for the lowest theta band [50]. Another, using spectral coherency profiles of microwire ECoG in motor cortex resulted in length scales from 0.8 to 1 mm at 150 Hz, and rising to 2.13–3.45 mm at low frequencies [49]. Raw correlogram profiles in STG recordings cross the 1/2 threshold between 1 and 3 mm in descending frequency bands [51]. Using device-independent covariance kernels (not scaled to signal or noise), we observed average half-correlation lengths with a minimum of ~ 1.15 mm in the HFB range for both brain areas, and a maximum in the alpha band of ~ 3 mm in pSTG and ~ 4.25 mm in motor cortex. The discrepancy between motor area findings may partially be due to the lack of distinction between ‘field’ and ‘signal’ in the correlation coefficient and coherency estimators. Spatially independent noise lowers normalized correlation values at all inter-electrode distances. Correlograms from the same neural field, but measured with different noise power, would show threshold crossings at different inter-electrode distances. Another factor in the present results that likely impacted correlation range in alpha and HFB was the state of general anesthesia under propofol [70]. Spatial correlation profiles are also highly variable across time, as observed in [51] and confirmed in this study.

Previous spatial spectra analyses identified effective bandwidths where physiological spectra intersected noise floors, and determined sufficient sampling densities in terms of the bandwidth reciprocal. Our median results for spatial bandwidth resolution were similar to previous findings in human [47] and rat [48]. However, we found that a field’s texture, which had a large impact on predictability, had only a subtle impact on the power spectrum, making bandwidth an unreliable estimator of sufficient sample spacing. In addition, the bandwidth selection methodology in this report eliminated device dependence by discarding the noise floor. Estimating bandwidth based on the intersection of field and noise spectra leads to the counter-intuitive result of decreased bandwidth/increased electrode spacing in low SNR scenarios and increased bandwidth/decreased spacing for higher SNR, when the underlying field spectrum might be equal. Our basic results suggest the opposite result (see figures 3(b)–(c)). The same neural field can be predicted to the same accuracy in low noise using

larger electrode spacing, or in high noise with smaller spacing.

The methodology we employed pre-supposed a need for correlated sampling, which is a requirement for spatial prediction. Another functional utility of redundant electrode signals was recently studied through the use of shared trial-to-trial variability in discriminating visual stimuli from V4 activity in NHP. Rather than being a nuisance, shared variability in LFP contributed substantially to decoding accuracy [76]. The logic of avoiding redundancy by setting electrode spacing based on spatial cycle limits was also challenged through a detection theory model that elucidated the impact of redundancy in both event-related signals of interest and background processes. High-density grids have greater detection power for spatially redundant event-related signals buried within a high-amplitude, low-correlation background process, or can conversely pick out spatially focal signals in the presence of highly correlated background activity [77]. The first result is directly analogous to our finding that field potential can be predicted to nominal precision in high noise with sufficiently dense sampling. The second result also relates to the need for dense sampling for highly textured (low smoothness) fields, even if the dominant correlation length scale is long range.

We attempted to adapt to nonstationarities in the field structure and SNR by operating in short-time batches. But there can be little doubt that our analysis smoothed over the most transient neural events such as evoked responses. We observed comparatively low fitness of our spatial prediction framework when kriging evoked response transients directly. Such events may plausibly be described by the superposition of uncorrelated background and response field process with different spatial covariance kernels, and thus may benefit from a nested variogram model [53].

The present analysis was indifferent to spatio-temporal interactions in the covariance kernel, which were clearly demonstrated empirically in [49] and are also indicated by the cortical traveling wave phenomenon [78]. The framework of spatial prediction can be expanded using appropriate spatio-temporal covariance kernels [79, 80]. It is quite likely that coupled structure in space and time may provide more efficient field potential prediction and reduce the sufficient sampling density indicated in this study.

The 95% ‘probable’ and 10% ‘approximate’ figures were chosen as intuitively grasped quantities for the purpose of exposition. However, in light of the results relating sampling predictability to mutual information with sensory stimulation (figure 6), the 10% error tolerance may be too large for most applications. In fact, tone classification accuracy from the passive arrays continued to improve until the smallest testable electrode spacing (i.e. the fully sampled grid). Expected error for 95% of the observed fields at 420 μm spacing would be 3% or less, and the

corresponding 95%–3% PAC sample spacing on the active array would be 69 μm . With these caveats in mind, the PAC sampling densities stated for multiple scenarios might be considered minimum starting points for electrophysiology in practice.

5. Conclusion

The present study attempted to rigorously address the problem of sufficient sampling in μECoG in terms of minimum MSE prediction of field potential. We introduced (a) a set of field covariance estimation techniques that improved upon common methodology in electrophysiology, and (b) a framework that quantified the relationship between prediction efficiency versus electrode spacing over a distribution of covariance and SNR conditions. Our prediction results suggested that sampling based on spatial bandwidth, as suggested in prior literature, can be a good rule of thumb for low frequency field potential and low noise conditions. However, using a single point estimate of bandwidth (i.e. the average) does not expose the full range of field statistics. Additional spatially over-sampling of the bandwidth-based pitch is required for rough textured fields, and can recover bandwidths beyond the noise floor in higher noise settings. We found that natural image statistics and SNR of field potential varied significantly within single recordings. Based on these distributions, we recommended sufficient sampling based on a high probability of low error predictions. These findings suggested that sufficient sample spacing for $\leq 10\%$ MSE predictability in noiseless conditions ranged from lows of $\sim 500 \mu\text{m}$ across species, up to 1.5 mm in low frequency human and NHP motor cortex. Accounting for the most adverse chronic implant noise conditions, sufficient sample spacings were reduced by 200–700 μm . Importantly, the observed prediction errors were matched by the expected error, allowing sufficient sampling inferences to be made based on reasonable parameter assumptions prior to future electrode design.

Funding

This work was funded by National Institute of Neurological Disorders and Stroke (NINDS) awards U01 NS099697 to JV, BP, and JAR and award R01 NS10493 to BP; a National Center for Advancing Translational Sciences (NCATS) award UL1TR002553 to Duke University, JV, and GC; a National Science Foundation award CCF1422914 to JV; a National Science Foundation award CCF-1564051 to JV; a NSF CAREER award CBET-1752274 to JV; a Steven W Smith Fellowship to BB; a L'Oreal USA for Women in Science Fellowship to ALO; and Defense Advanced Research Programs Agency awards DARPA-BAA-16-09 to BP, JAR, and JV, and DARPA-BAA-13-20 to BP, JAR, and JV, and

SUBNETS program cooperative agreement W911NF-14-2-0043, BTO contract HR0011-14-C-0102, and NESD program contract N66001-17-C-4002 to BP.

Conflict of interest

Parts of the technology described here are patented under ‘Conformable Actively Multiplexed High-Density Surface Electrode Array for Brain Interfacing,’ U.S. Patent No. 8934965; ‘Flexible and Scalable Sensor Arrays for Recording and Modulating Physiologic Activity,’ U.S. Patent Nos. 9107592 and 9839367, and European Patent No. 2265171; and ‘Conformable Actively Multiplexed High-Density Surface Electrode Array for Brain Interfacing,’ U.S. Patent No. 10349860; and ‘Electroencephalography (EEG) Electrode Arrays and Related Methods of Use,’ U.S. Patent No. PCT/US2020/051400. The authors declare that they have no other competing interests.

ORCID iDs

Michael Trumpis  <https://orcid.org/0000-0002-3834-4437>

Chia-Han Chiang  <https://orcid.org/0000-0002-4010-1266>

Amy L Orsborn  <https://orcid.org/0000-0003-4131-5781>

Brinnae Bent  <https://orcid.org/0000-0002-7039-0177>

Bijan Pesaran  <https://orcid.org/0000-0003-4116-0038>

Gregory Cogan  <https://orcid.org/0000-0003-1557-6507>

Jonathan Viventi  <https://orcid.org/0000-0001-6054-0541>

References

- [1] Jasper H and Penfield W 1949 Electrocorticograms in man: effect of voluntary movement upon the electrical activity of the precentral gyrus *Arch. für Psychiatr. Nervenkrankheiten* **183** 163–74
- [2] Pei X, Leuthardt E C, Gaona C M, Brunner P, Wolpaw J R and Schalk G 2011 Spatiotemporal dynamics of electrocorticographic high gamma activity during overt and covert word repetition *Neuroimage* **54** 2960–72
- [3] Pasley B N, David S V, Mesgarani N, Flinker A, Shamma S A, Crone N E, Knight R T and Chang E F 2012 Reconstructing speech from human auditory cortex *PLoS Biol.* **10** e1001251
- [4] Chestek C A, Gilja V, Blabe C H, Foster B L, Shenoy K V, Parvizi J and Henderson J M 2013 Hand posture classification using electrocorticography signals in the gamma band over human sensorimotor brain areas *J. Neural Eng.* **10** 026002
- [5] Miller K J, Honey C J, Hermes D, Rao R P N, denNijs M and Ojemann J G 2014 Broadband changes in the cortical surface potential track activation of functionally diverse neuronal populations *NeuroImage* **85** 711–20
- [6] Cogan G B, Thesen T, Carlson C, Doyle W, Devinsky O and Pesaran B 2014 Sensory–motor transformations for speech occur bilaterally *Nature* **507** 94–98
- [7] Cogan G B, Iyer A, Melloni L, Thesen T, Friedman D, Doyle W, Devinsky O and Pesaran B 2017 Manipulating

- stored phonological input during verbal working memory *Nat. Neurosci.* **20** 279
- [8] Akbari H, Khalighinejad B, Herrero J L, Mehta A D and Mesgarani N 2019 Towards reconstructing intelligible speech from the human auditory cortex *Sci. Rep.* **9** 874
- [9] Anumanchipalli G K, Chartier J and Chang E F 2019 Speech synthesis from neural decoding of spoken sentences *Nature* **568** 493–8
- [10] Wang Xi et al 2017 Mapping the fine structure of cortical activity with different micro-ECoG electrode array geometries *J. Neural Eng.* **14** 056004
- [11] Wang W et al 2009 Human motor cortical activity recorded with micro-ECoG electrodes, during individual finger movements *Engineering in Medicine and Biology Society, 2009. EMBC 2009. Annual Int. Conf. IEEE (IEEE)* pp 586–9
- [12] Kellis S, Miller K, Thomson K, Brown R, House P and Greger B 2010 Decoding spoken words using local field potentials recorded from the cortical surface *J. Neural Eng.* **7** 056007
- [13] Moses D A, Mesgarani N, Leonard M K and Chang E F 2016 Neural speech recognition: continuous phoneme decoding using spatiotemporal representations of human cortical activity *J. Neural Eng.* **13** 056004
- [14] Muller L, Felix S, Shah K G, Lee K, Pannu S and Chang E F 2016 Thin-film, high-density micro-electrocorticographic decoding of a human cortical gyrus 2016 38th Annual Int. Conf. IEEE Engineering in Medicine and Biology Society (EMBC) pp 1528–31
- [15] Tang C, Hamilton L S and Chang E F 2017 Intonational speech prosody encoding in the human auditory cortex *Science* **357** 797–801
- [16] Leuthardt E C, Freudenberg Z, Bundy D and Roland J 2009 Microscale recording from human motor cortex: implications for minimally invasive electrocorticographic brain–computer interfaces *Neurosurg. Focus* **27** E10
- [17] Wang P T et al 2016 Comparison of decoding resolution of standard and high-density electrocorticogram electrodes *J. Neural Eng.* **13** 026016
- [18] Flint R D, Rosenow J M, Tate M C and Slutzky M W 2017 Continuous decoding of human grasp kinematics using epidural and subdural signals *J. Neural Eng.* **14** 016005
- [19] Ramsey N F, Salari E, Aarnoutse E J, Vansteensel M J, Bleichner M G and Freudenberg Z V 2018 Decoding spoken phonemes from sensorimotor cortex with high-density ECoG grids *Neuroimage* **180** 301–11
- [20] Park D-W et al 2014 Graphene-based carbon-layered electrode array technology for neural imaging and optogenetic applications *Nat. Commun.* **5** 5258
- [21] Khodagholy D, Gelinias J N, Thesen T, Doyle W, Devinsky O, Malliaras G G and Buzsáki G 2014 NeuroGrid: recording action potentials from the surface of the brain *Nat. Neurosci.* **18** 310–5
- [22] Yu K J et al 2016 Bioresorbable silicon electronics for transient spatiotemporal mapping of electrical activity from the cereb. cortex *Nat. Mater.* **15** 782–91
- [23] Insanally M, Trumpis M, Wang C, Chiang C-H, Woods V, Palopoli-Trojani K, Bossi S, Froemke R C and Viventi J 2016 A low-cost multiplexed μ ECoG system for high-density recordings in freely moving rodents *J. Neural Eng.* **13** 026030
- [24] Ganji M et al 2017 Development and translation of PEDOT: PSS microelectrodes for intraoperative monitoring *Adv. Funct. Mater.* **28** 1700232
- [25] Diaz-Botia C A, Luna L E, Neely R M, Chamanzar M, Carraro C, Carmena J M, Sabes P N, Maboudian R and Maharbiz M M 2017 A silicon carbide array for electrocorticography and peripheral nerve recording *J. Neural Eng.* **14** 056006
- [26] Fang H et al 2017 Capacitively coupled arrays of multiplexed flexible silicon transistors for long-term cardiac electrophysiology *Nat. Biomed. Eng.* **1** 0038 E
- [27] Chiang C-H et al 2020 Development of a neural interface for high-definition, long-term recording in rodents and nonhuman primates *Sci. Trans. Med.* **12** eaay4682
- [28] Lacour Sephanie P, Courtine Gegoire and Guck J 2016 Materials and technologies for soft implantable neuroprostheses *Nat. Rev. Mater.* **1** 16063
- [29] Hong G and Lieber C M 2019 Novel electrode technologies for neural recordings *Nat. Rev. Neurosci.* **20** 330–45
- [30] Barth D S 2003 Submillisecond synchronization of fast electrical oscillations in neocortex *J. Neurosci.* **23** 2502–10
- [31] Escabi M A et al 2014 A high-density, high-channel count, multiplexed μ ECoG array for auditory-cortex recordings *J. Neurophysiol.* **112** 1566–83
- [32] Trumpis M, Insanally M, Zou J, Elsharif A, Ghomashchi A, Sertac Artan N, Froemke R C and Viventi J 2017 A low-cost, scalable, current-sensing digital headstage for high channel count μ ECoG *J. Neural Eng.* **14** 026009
- [33] Kaiju T et al 2017 High spatiotemporal resolution ECoG recording of somatosensory evoked potentials with flexible micro-electrode arrays *Front. Neural Circuits* **11** 20
- [34] Viventi J et al 2011 Flexible, foldable, actively multiplexed, high-density electrode array for mapping brain activity in vivo *Nat. Neurosci.* **14** 1599–605
- [35] Toda H, Suzuki T, Sawahata H, Majima K, Kamitani Y and Hasegawa I 2011 Simultaneous recording of ECoG and intracortical neuronal activity using a flexible multichannel electrode-mesh in visual cortex *Neuroimage* **54** 203–12
- [36] Sahasrabudhe K et al 2020 The Argo: A high channel count recording system for neural recording in vivo *J. Neural Eng.* (<https://doi.org/10.1088/1741-2552/abd0ce>)
- [37] Ramirez H L, Steudel S and Haesler S et al 2019 Neurofabric–flexible electrical interfaces for high-density epicortical recordings based on metal oxide thin-film transistor 2019 *IEEE Conf. Neural Engineering* (San Francisco)
- [38] Katzner S, Nauhaus I, Benucci A, Bonin V, Ringach D L and Carandini M 2009 Local origin of field potentials in visual cortex *Neuron* **61** 35–41
- [39] Xing D, Yeh C-I and Shapley R M 2009 Spatial spread of the local field potential and its laminar variation in visual cortex *J. Neurosci.* **29** 11540–9
- [40] Markowitz D A, Wong Y T, Gray C M and Pesaran B 2011 Optimizing the decoding of movement goals from local field potentials in macaque cortex *J. Neurosci.* **31** 18412–22
- [41] Lindén H, Tetzlaff T, Potjans T C, Pettersen K H, Grün S, Diesmann M and Einevoll G T 2011 Modeling the spatial reach of the LFP *Neuron* **72** 859–72
- [42] Łęski S, Lindén H, Tetzlaff T, Pettersen K H and Einevoll G T 2013 Frequency dependence of signal power and spatial reach of the local field potential *PLoS Comput. Biol.* **9** e1003137
- [43] Richner T J, Thongpang S, Brodnick S K, Schendel A A, Falk R W, Thongpang S, Brodnick S K, Schendel A A, Pashaie R and Williams J C 2014 Optogenetic micro-electrocorticography for modulating and localizing cerebral cortex activity *J. Neural Eng.* **11** 016010
- [44] Ledochowitsch P et al 2015 Strategies for optical control and simultaneous electrical readout of extended cortical circuits *J. Neurosci. Methods* **256** 220–31
- [45] Yazdan-Shahmorad A, Diaz-Botia C, Hanson T L, Kharazia V, Ledochowitsch P, Maharbiz M M and Sabes P N 2016 A large-scale interface for optogenetic stimulation and recording in nonhuman primates *Neuron* **89** 927–39
- [46] Barrie J M, Freeman W J and Lenhart M D 1996 Spatiotemporal analysis of prepyriform, visual, auditory and somesthetic surface EEGs in trained rabbits *J. Neurophysiol.* **76** 520–39
- [47] Freeman W J, Rogers L J, Holmes M D and Silbergeld D L 2000 Spatial spectral analysis of human electrocorticograms including the alpha and gamma bands *J. Neurosci. Methods* **95** 111–21
- [48] Slutzky M W, Jordan L R, Krieg T, Chen M, Mogul D J and Miller L E 2010 Optimal spacing of surface electrode arrays

- for brain–machine interface applications *J. Neural Eng.* **7** 026004
- [49] Kellis S, Sorensen L, Darvas F, Sayres C, O'Neill K, Brown R B, House P, Ojemann J and Greger B 2016 Multi-scale analysis of neural activity in humans: implications for micro-scale electrocorticography *Clin. Neurophysiol.* **127** 591–601
- [50] Muller L, Hamilton L S, Edwards E, Bouchard K E and Chang E F 2016 Spatial resolution dependence on spectral frequency in human speech cortex electrocorticography *J. Neural Eng.* **13** 056013
- [51] Rogers N et al 2019 Correlation structure in micro-ECoG recordings is described by spatially coherent components *PLoS Comput. Biol.* **15** e1006769
- [52] Cressie N 1990 The origins of kriging *Math. Geol.* **22** 239–52
- [53] Wackernagel H 2003 *Multivariate Geostatistics* (Berlin: Springer) (<https://doi.org/10.1007/978-3-662-05294-5>)
- [54] Rasmussen C E 2004 *Gaussian processes in machine learning Advanced Lectures on Machine Learning* (Berlin: Springer) 63–71
- [55] Woods V et al 2018 Long-term recording reliability of liquid crystal polymer μ ECoG arrays *J. Neural Eng.* **15** 066024
- [56] Jinghua Li et al 2018 Conductively coupled flexible silicon electronic systems for chronic neural electrophysiology *Proc. Natl Acad. Sci.* **115** E9542–9
- [57] Bink H, Wagenaar J B and Viventi J 2013 Data acquisition system for high resolution, multiplexed electrode arrays 2013 6th Int. IEEE/EMBS Conf. Neural Engineering (NER) (IEEE) pp 1001–4
- [58] Siegle J H, Hale G J, Newman J P and Voigts J 2015 Neural ensemble communities: open-source approaches to hardware for large-scale electrophysiology *Curr. Opin. Neurobiol.* **32** 53–9
- [59] Kleinbart J E, Orsborn A L, Choi J S, Wang C, Qiao S, Viventi J and Pesaran B 2018 A modular implant system for multimodal recording and manipulation of the primate brain 2018 40th Annual Int. Conf. IEEE Engineering in Medicine and Biology Society (EMBC) pp 3362–5
- [60] Zimmerman D L and Stein M 2010 *Classical Geostatistical Methods Handbook of Spatial Statistics* (Boca Raton, FL: CRC Press) pp 29–44
- [61] Rasmussen C E 2006 *Gaussian Processes for Machine Learning* (Cambridge, MA: MIT Press)
- [62] Gavish M and Donoho D L 2014 The optimal hard threshold for singular values is $4/\sqrt{3}$ *IEEE Trans. Inf. Theory* **60** 5040–53
- [63] Wilcox R R 2011 *Introduction to Robust Estimation and Hypothesis Testing* 3rd (Cambridge, MA: Academic Press)
- [64] Manning J R, Jacobs J, Fried I and Kahana M J 2009 Broadband shifts in local field potential power spectra are correlated with single-neuron spiking in humans *J. Neurosci.* **29** 13613–20
- [65] Ray S and Maunsell J H R 2011 Different origins of gamma rhythm and high-gamma activity in macaque visual cortex *PLoS Biol.* **9** e1000610
- [66] Miller K J, Zanos S, Fetz E E, den Nijs M and Ojemann J G 2009 Decoupling the cortical power spectrum reveals real-time representation of individual finger movements in humans *J. Neurosci.* **29** 3132–7
- [67] Bridson R 2007 *Fast Poisson disk sampling in arbitrary dimensions ACM SIGGRAPH 2007 Sketches (New York, NY) (ACM)* (<https://doi.org/10.1145/1278780.1278807>)
- [68] Hanneke S 2016 The optimal sample complexity of PAC learning *J. Mach. Learn. Res.* **17** 1319–33
- [69] Olea R A 2006 A six-step practical approach to semivariogram modeling *Stoch. Environ. Res. Risk Assessment* **20** 307–18
- [70] Purdon P L et al 2013 Electroencephalogram signatures of loss and recovery of consciousness from propofol *Proc. Natl Acad. Sci.* **110** E1142–51
- [71] Sekihara K, Nagarajan S S, Poeppel D, Marantz A and Miyashita Y 2001 Reconstructing spatio-temporal activities of neural sources using an meg vector beamformer technique *IEEE Trans. Biomed. Eng.* **48** 760–71
- [72] Lin F-H, Witzel T, Ahlfors S P, Stufflebeam S M, Belliveau J W and Hämäläinen M S 2006 Assessing and improving the spatial accuracy in MEG source localization by depth-weighted minimum-norm estimates *Neuroimage* **31** 160–71
- [73] Grech R, Cassar T, Muscat J, Camilleri K P, Fabri S G, Zervakis M, Xanthopoulos P, Sakkalis V and Vanrumste B 2008 Review on solving the inverse problem in EEG source analysis *J. Neuroeng. Rehabil.* **5** 25
- [74] Foldes S T and Taylor D M 2011 Offline comparison of spatial filters for two-dimensional movement control with noninvasive field potentials *J. Neural Eng.* **8** 046022
- [75] Bradley J R, Cressie N and Shi T 2016 A comparison of spatial predictors when datasets could be very large *Statist. Surv.* **10** 100–31
- [76] Foroushani A N, Neupane S, Pastor P D H, Pack C C and Sawan M 2020 Spatial resolution of local field potential signals in macaque v4 *J. Neural Eng.* **17** 026003
- [77] Hermiz J, Rogers N, Kaestner E, Mehran Ganji D R, Cleary B C, Barba D, Dayeh S, Halgren E and Gilja V 2018 Sub-millimeter ECoG pitch in human enables higher fidelity cognitive neural state estimation *NeuroImage* **176** 454–64
- [78] Muller L, Chavane F eric, Reynolds J and Sejnowski T J 2018 Cortical travelling waves: mechanisms and computational principles *Nat. Rev. Neurosci.* **19** 255–68
- [79] Stein M L 2005 Space–time covariance functions *J. Am. Stat. Assoc.* **100** 310–21
- [80] Cressie N and Wikle C K 2011 *Statistics for Spatio-Temporal Data* (New York: Wiley)